Universitat Autònoma de Barcelona

Dipòsit digital de documents de la UAB

This is the **accepted version** of the article:

Martins, Sofia; de Rojas, Julius; Tan, Zhengwei; [et al.]. «Dynamic electric-field-induced magnetic effects in cobalt oxide thin films : towards magneto-ionic synapses». Nanoscale, Vol. 14, Issue 3 ((January 2022), p. 842-852. DOI 10.1039/D1NR06210G

This version is available at https://ddd.uab.cat/record/250399

under the terms of the IN COPYRIGHT license

Dynamic electric-field-induced magnetic effects in cobalt oxide thin films: towards magneto-ionic synapses

Sofia Martins[a], Julius de Rojas[a], Zhengwei Tan[ab], Matteo Cialone[b], Aitor Lopeandia[c], Javier Herrero-Martín[d], José L. Costa-Krämer[e], Enric Menéndez*[a] and Jordi Sort*[af]

[a]*Departament de Física, Universitat Autònoma de Barcelona, E-08193 Cerdanyola del Vallès, Spain. E-mail: Enric.Menendez@uab.cat; Jordi.Sort@uab.cat*
[b]*CNR-SPIN Genova, C.so F. M. Perrone 24, Genova, 16152, Italy*
[c]*Catalan Institute of Nanoscience and Nanotechnology (ICN2), CSIC and BIST, Campus UAB, Cerdanyola del Vallès, E-08193 Barcelona, Spain*
[d]*ALBA Synchrotron Light Source, 08290 Cerdanyola del Vallès, Spain*
[e]*IMN-Instituto de Micro y Nanotecnología (CNM-CSIC), Isaac Newton 8, PTM, 28760 Tres Cantos, Madrid, Spain*
[f]*Institució Catalana de Recerca i Estudis Avançats (ICREA), Pg. Lluís Companys 23, E-08010 Barcelona, Spain*

Abstract

Voltage control of magnetism *via* electric-field-driven ion migration (magneto-ionics) has generated intense interest due to its potential to greatly reduce heat dissipation in a wide range of information technology devices, such as magnetic memories, spintronic systems or artificial neural networks. Among other effects, oxygen ion migration in transition-metal–oxide thin films can lead to the generation or full suppression of controlled amounts of ferromagnetism ('ON–OFF' magnetic transitions) in a non-volatile and fully reversible manner. However, oxygen magneto-ionic rates at room temperature are generally considered too slow for industrial applications. Here, we demonstrate that sub-second ON–OFF transitions in electrolyte-gated paramagnetic cobalt oxide films can be achieved by drastically reducing the film thickness from >200 nm down to 5 nm. Remarkably, cumulative magneto-ionic effects can be generated by applying voltage pulses at frequencies as high as 100 Hz. Neuromorphic-like dynamic effects occur at these frequencies, including potentiation (cumulative magnetization increase), depression (*i.e.*, partial recovery of magnetization with time), threshold activation, and spike time-dependent magnetic plasticity (learning and forgetting capabilities), mimicking many of the biological synapse functions. The systems under investigation show features that could be useful for the design of artificial neural networks whose magnetic properties would be governed with voltage.

Introduction

With the advent of Big Data, current computational architectures are proving to be insufficient.[1] Miniaturization of complementary metal–oxide semiconductor (CMOS) technologies (Moore's law) is starting to show signs of deceleration because of the difficulties in decreasing transistor size below 10 nm,[2] while the areal density in hard disk drives (HDDs) is also limited by the superparamagnetic effect, relying on technologies such as heat assisted magnetic recording (HAMR) to reduce bit sizes.[3] In addition, increasingly complex algorithms need to be performed in a much faster and energy-efficient manner. This is not easy in the current von Neumann computer architecture, in which the mass storage sub-device (*e.g.*, HDD) is placed separately from the data processing unit and the random-access memory (RAM) that keep data in read-write mode. The shuffling of data between the processing unit and the memories results in large power consumption[4] and computational speeds that are limited by the frequency at which the memory sub-devices can transfer data to the processing unit.[5]

To meet the demands of artificial intelligence and the Internet of Things, a new brain-inspired computation paradigm, neuromorphic computing, has emerged as an alternative. Neuromorphic computing emulates the activity of biological synapses by utilizing artificial neural networks in which synapses are massively interconnected in a dynamic and reconfigurable way to process information in an energy-efficient manner.[6–9] Although the bases of this computation paradigm were formulated in the 1990s,[8,10] a renewed interest has emerged in recent years, jump-started by the discovery and development of advanced materials that might address some of the essential requirements of brain-inspired computing. So far, emulation of artificial synapses has been achieved, to some extent, using phase change materials,[11] superconductors,[12] transistors,[13] spintronic devices[14,15] andmemristors.[16,17] However, meeting technical requirements such as room-temperature operation, high speeds, chip integration/compatibility and low power consumption remains a challenge.[18] Many of the above-mentioned materials are ultimately controlled by electric currents, which involve significant energy loss by heat dissipation through the Joule effect and the associated cooling requirements.

In recent years, voltage control of magnetism has attracted intense research interest because it has the potential to drastically decrease energy consumption, thereby rendering ultra-low-power data storage.[19–22] While magnetoelectric actuation protocols have been proposed as an alternative to thermally-assisted magnetic recording and in new designs of random-access memories, research on the use of this effect for neuromorphic computing is promising but still in early stages.[23,24] Yet, two important advantages of magnetoelectric designs over memristor-like materials, besides energy efficiency, are envisioned:[23] the use of different read/write paths (which avoids interference between synapses during the read operation), and the possibility to induce negative synaptic weights, taking advantage of the fact that magnetization is a vector, whereas electrical conductance is a scalar quantity. This allows the synapse to be programmed with either excitatory signals (*via* a positive weight) or inhibitory signals (*via* a negative weight), mimicking the brains capability to increase/decrease the membrane potential of postsynaptic neurons under certain conditions. So far, electric-field control of magnetism has primarily relied on the following strategies:[19] (i) the use of single-phase multiferroic materials with intrinsic magnetoelectric coupling,[25,26] (ii)

electric charge accumulation in ferromagnetic metals or semiconductors[27,28] and (iii) piezostrain-mediated effects through inverse magnetostriction in ferromagnetic/ferroelectric heterostructures.[29–31] The implementation of these approaches in marketable devices is hampered by several factors. Intrinsic multiferroics are scarce and show relatively weak magnetoelectric coupling at room temperature. The penetration of an applied electric-field (*i.e.*, electronic charging) in metallic or semiconducting ferromagnets is limited to the very outer surface (screening length in metals is around 5 Å), thus imposing strong thickness restrictions on the actuated materials. Finally, artificial multiferroic ferromagnetic/ferroelectric heterostructures suffer from fatigue effects, clamping effects when grown onto a rigid substrate, and high voltage requirements when the ferromagnetic layer is directly grown onto a ferroelectric substrate. Even though clamping effects would be minimized by using flexible polymer-based ferroelectrics, the capacity of piezostrain-mediated effects to modulate magnetic properties is more limited than that of magneto-ionics.

An alternative to the above mechanisms is the use of an applied electric-field to induce ion migration effects that modify the magnetic properties of materials (magneto-ionics).[32–42] Magneto-ionics can extend to the bulk (beyond the outer surface of target films), induces non-volatile (*i.e.*, permanent) changes in the magnetic properties, and has been reported to be highly energy efficient. Magneto-ionics involves write/delete energies per bit lower than 10^{-3} pJ per bit.[43,44] This represents energies several orders of magnitude lower than those required by memristors (10^{-1} pJ per bit), conventional toggle MRAMs (1 pJ per bit), or HDDs (>10^{3} pJ per bit).[45–47] However, magneto-ionic motion of oxygen at room temperature is usually rather slow, involving several seconds or even minutes to toggle the magnetic state. Since ion migration is a thermally activated process, magneto-ionic rates can be accelerated if the system is heated while voltage is applied, but at the cost of reduced energy efficiency. Recently, *via* a proton-based approach (*i.e.*, H^+ ion migration),[33,34] 10^{-3} s room-temperature operation has been shown in yttria-stabilized zirconia/Pd/Co heterostructures.[33] This approach is very appealing, but still needs further optimization to increase hydrogen retention and make the system less dependent on environmental humidity.

The use of pristine ferromagnetic layers (*e.g.*, Co, Ni or Fe) as starting materials grown adjacent to ionic conductors (*e.g.*, HfO_2, GdO_x, Al_2O_3) poses some drawbacks. First, it is often difficult to achieve a fully OFF state (*i.e.*, full oxidation) by voltage application; the most frequently reported effect is a voltage-induced reorientation of the magnetic easy axis. Second, when the metal is oxidized, pronounced structural changes (*i.e.*, phase transformations) take place, leading to irreversible structural effects and, thus, poor cyclability and endurance. An alternative approach is to use target materials whose crystal structure already contains the ions to be transported (*i.e.*, magneto-ionic targets such as Co_3O_4 [35,37] or CoN[36,48] to transport oxygen or nitrogen, respectively). Such magneto-ionic targets can undergo fully reversible transformations from a non-ferromagnetic (OFF) to a ferromagnetic (ON) state and *vice versa*, just by the generation of atomic vacancies.[35–37] This has been demonstrated at room temperature in electrolyte-gated paramagnetic Co_3O_4 and CoN films. In our previous works, we investigated relatively thick (≥85 nm) layers, which took several minutes to generate a magnetic moment equal to few % of the saturation magnetization of bulk metallic Co.[35–37]

Here, we show novel results in electrolyte-gated thin cobalt oxide layers at room temperature using static (DC) and pulsed voltage. By reducing the cobalt oxide layer thickness down to 5 nm, sub-second ON–OFF magnetic transformations are demonstrated. Remarkably, through application of pulsed voltage functions, activation times of 10^{-2} s can be inferred. At such frequencies, the investigated material shows some interesting neuromorphic functionalities, such as cumulative (learning) and relaxation (forgetting) time-dependent magnetization dependences, under suitable voltage conditions.

Experimental

2.1. Sample preparation

Cobalt oxide films were grown at room temperature on Si/Ti/Cu substrates (*i.e.*, Cu (60 nm)/Ti (20 nm)/〈100〉Si (725 μm)) by reactive sputtering using a cobalt target as Co precursor and O_2 plasma as oxygen source. Argon was used as a carrier gas for the Co precursor. The deposition was performed with an AJA International, Inc. Magnetron Sputtering System ATC Orion with a base pressure of 10^{-7} mbar. Sputtering was conducted using a DC gun applying 200 W. The deposition rate was 23 nm min^{-1}. The adhesive (Ti) and seed (Cu) layers were also grown by sputtering using the same experimental setup but in an inert atmosphere. Cu wires were welded to the electrodes using indium. Insulating hot glue spacers were used to avoid short-circuits.

2.2. Structural measurements

ϑ–2ϑ X-ray diffraction (XRD) patterns of the different samples were recorded on a Philips XPert Powder diffractometer using Cu Kα radiation. The structural parameters of films, such as crystallite size (*i.e.*, average coherently diffracting domain), lattice parameters or microstrains were evaluated by fitting the XRD patterns using the MAUD Rietveld refinement software. High-resolution transmission electron microscopy (HRTEM) was performed on a TECNAI F20 HRTEM/STEM microscope operated at 200 kV. A cross sectional lamella was prepared by focused ion beam and placed onto a Cu transmission electron microscopy grid.

2.3. Compositional measurements

X-ray absorption spectroscopy (XAS) were investigated at the Co $L_{2,3}$ edges in BL29-BOREAS beamline at ALBA Synchrotron Light Source (Barcelona, Spain).[49] The spectra were measured in total electron yield (TEY) mode, under ultra high vacuum conditions (2×10^{-10} mbar) and at room temperature (300 K). The applied magnetic field (parallel to the X-ray beam) was 6 T, with the magnetic field along in-plane direction forming an angle of 30° with the film surface.

2.4. Magnetoelectric characterization

Magnetic measurements under electrolyte gating were carried out at room temperature in a vibrating sample magnetometer (VSM) from Micro Sense (LOT-Quantum Design),

with a maximum in-plane applied magnetic field of 2 T in samples with electrochemical capacitor configuration, where the working electrode is made on the exposure copper beside to the cobalt oxide layer using the experimental setup as illustrated in Fig. S1† and described in the text. The static and time-dependent magnetic measurements by VSM are given as magnetization M (emu cm^{-3}) *vs.* applied magnetic field H (Oe) and magnetization M (emu cm^{-3}) *vs.* time t (h), respectively. To give M in T, the M values given in emu cm^{-3} should be first multiplied by 1000 to obtain M in A m^{-1}, and then by μ_0 ($\mu_0 = 4\pi \times 10^{-7}$ N A^{-2}): $\mu_0 M$ (T) = $4\pi \times 10^{-4} M$ (emu cm^{-3}). Additionally, the applied magnetic field H can also be given in T (or in mT since T is a rather large unit) if the H values given in Oe are transformed to A m^{-1} (by multiplying by 1000/(4π)), and then multiplied by μ_0 ($\mu_0 = 4\pi \times 10^{-7}$ N A^{-2})): $\mu_0 H$ (mT) = $10^{-1} H$ (Oe). The magnetic properties were recorded both for the pristine as-grown films and after applying voltage for different times, frequencies and magnetic fields. An Agilent B2902A power supply was used to generate the voltage functions. All magnetoelectric measurements were performed by immersing the sample in propylene carbonate (with traces of Na^+ dissolved) and using a platinum wire as counter electrode.[21,35] Taking into account that M *vs.* H measurements start from positive saturation at 20 000 Oe, the coercivity H_C is taken when the magnetization equals 0 for consecutive descending and ascending magnetic field sweeping branches. The saturation magnetization M_S is determined, upon linear contributions are subtracted, as the value of magnetization at applied magnetic fields of 10 000 Oe and 10 000 Oe for each descending and ascending hysteresis loop branches. For the negative parts of the branches, the absolute value of M_S is considered.

Results and discussion

Paramagnetic, semiconducting cobalt oxide films were grown by reactive sputtering on [100]-oriented Si substrates previously coated with Ti (20 nm) and Cu (60 nm) as buffer layers to serve as a working electrode for the voltage actuation. To investigate the role of thickness on the resulting magneto-ionic behavior, a series of cobalt oxide film, ranging from 5 to 230 nm in thickness, were prepared (see Experimental section). To assess the crystalline phases present in the films (as well as the crystallite size and microstrains), the as-grown samples were structurally characterized by XRD. XAS at room temperature was used to characterize the elemental composition and oxidation state of the cobalt oxide films.

As shown in Fig. 1a, besides the peaks from the Si substrate (grey curve), the cobalt oxide films give rise to clear additional diffraction peaks. Peaks with angular positions compatible with the (111), (311) and (222) directions of Co_3O_4 (PDF 00-009-0418) are observed in the XRD patterns corresponding to the thick (*e.g.*, 230 nm) films (black curve), evidencing polycrystallinity. Note that some diffraction peaks (*e.g.*, the (220) peak, which should appear ≈31°) are not observed, indicating some degree of crystallographic texture. This is in agreement with the tendency of Co_3O_4 to grow with columnar-shaped grains.[35] However, the presence of (111) and (222) XRD peaks unambiguously indicate the formation of Co_3O_4 rather than CoO. The 36 nm-thick films show only a single XRD peak around 2ϑ = 36.5° which is compatible with the position of both the (311) Co_3O_4 and the (111) CoO (PDF 00-001-1227) crystallographic phases. Note that no peak is observed at 42° (which would correspond to (200) CoO) for 230 nm

thick sample. As can be seen in Fig. 1b, the XAS spectra of the 5 and 15 nm thick films consists of one multiplet peak near 775 eV, followed by the splitting of the main peak into three sub-peaks, along with a shoulder at 780 eV. These first three peaks (labeled 1, 2, 3 in Fig. 1b) can be associated with the Co^{2+} valence state, and it is consistent with CoO.[50,51] For the 36 nm thick film, 2^+ and 3^+ oxidation states of Co are observed and, for the 230 nm thick film, the contribution of 3^+ oxidation state increases further, as evidenced by the relative decrease in multiplet peak intensity (1, 2 and 3) relative to the main peak (4) and the broadening of the shoulder (5), consistent with the presence of Co^{3+} in a Co_3O_4 phase.[50] From Rietveld refinements of the XRD patterns, the extracted values of the smallest crystallite size are 33 ± 5 nm and 63 ± 5 nm for the 36 nm and 230 nm thick cobalt oxide films, respectively, revealing that the 36 nm thick films mainly comprise a single layer of crystallites along the thickness of the film, whereas the 230 nm thick films also show polycrystallinity along the film thickness. The microstrains are of the order of 60×10^{-4} and 2×10^{-4} for the thinner and thicker films, respectively, in agreement with a slightly more strained cobalt oxide phase of the 36 nm thick film since the crystallites extend over the whole thickness without dividing and, accumulating certain strain. The XRD and XAS data reveal a transition from CoO to Co_3O_4 as a function of thickness: ranging from CoO to Co_3O_4 for the 5 and 230 nm thick films, respectively. The growth of Co_3O_4 in the thickest films indicates that, while reactive sputtering, the oxygen partial pressure is high enough to grow highly oxidized Co compounds, such as Co_3O_4. Conversely, for the thinnest films, CoO instead of Co_3O_4 is formed, suggesting that the Cu buffer layer might suffer from oxidation, resulting in a decreased effective oxygen partial pressure near the surface, which leads to the formation of a less oxidized cobalt oxide, such as CoO. With increasing thickness, traces of Co^{3+} oxidation state become more pronounced, indicating that coppers role in oxygen capture extends only to the first nm, allowing for more oxidizing conditions as the film continues to grow and, thus, forming Co_3O_4.[52,53] To investigate the role of thickness on the magneto-ionic ion motion and cyclability of cobalt oxide films, samples were magnetoelectrically characterized by VSM during electrolyte-gating (Fig. S1†). Specifically, the heterostructures were immersed in propylene carbonate, which is a aprotic polar anhydrous electrolyte which can dissolve O and, thus, capable of sinking/sourcing O^{2-} ions.[35] A Pt wire was used as counter electrode.

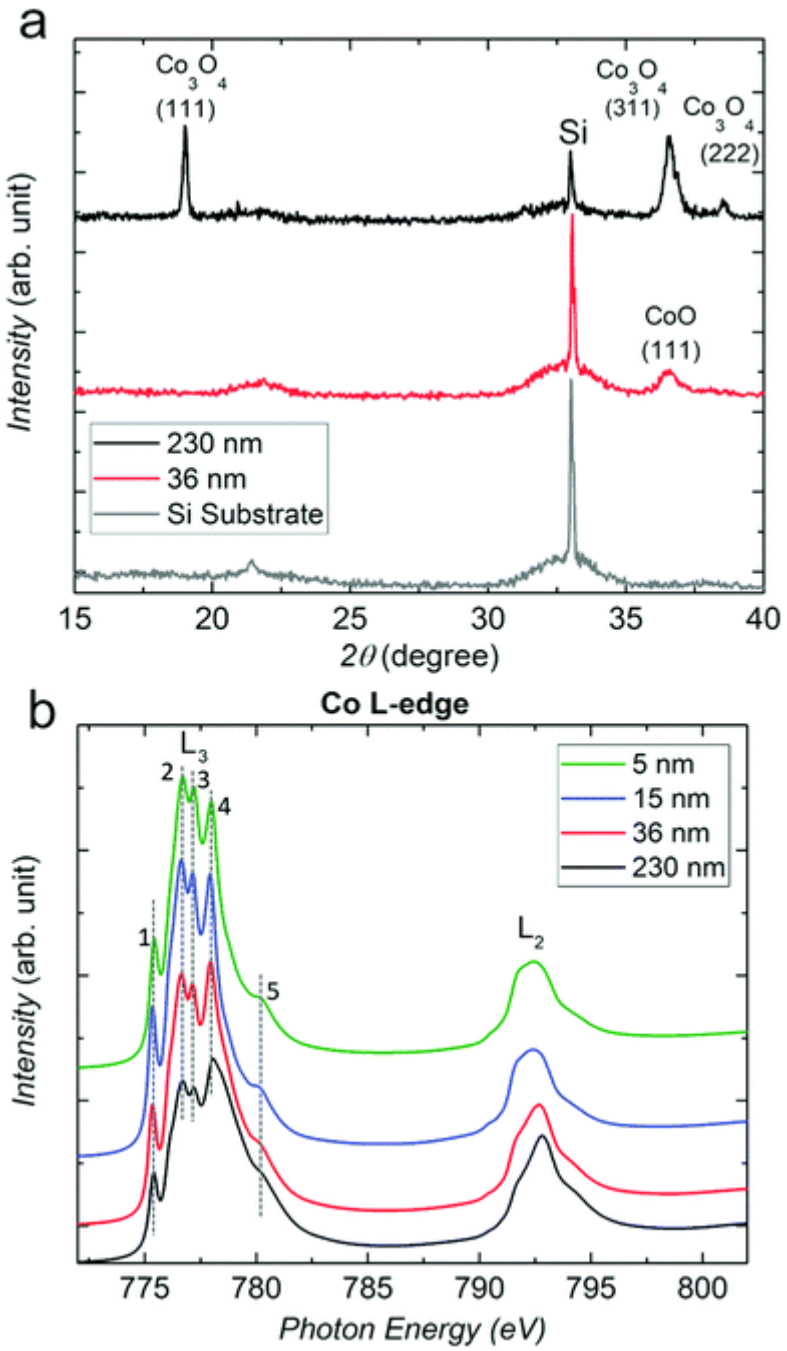

Fig. 1 (a) ϑ–2ϑ XRD patterns of cobalt oxide films (36 nm and 230 nm thick) and a bare Cu/Ti/Si substrate. (b) Co $L_{2,3}$-edge XAS of the 5, 15, 36 and 230 nm thick cobalt oxide films.

When voltage is applied, an electric double layer (EDL) forms at the interface between cobalt oxide films and the electrolyte which, due to its narrow thickness, allows the generation of large electric-fields perpendicular to the surface of the films (see Fig. S2†).[21]

The samples were subjected to −50 V for several hours and in-plane magnetic hysteresis loops of 35 min duration each were continuously recorded. The first, second and fifteenth hysteresis loops, for four different cobalt oxide thicknesses, together with

the hysteresis loops of the as-prepared films, are shown in Fig. 2. Note that the as-prepared cobalt oxide films are virtually non-ferromagnetic, as it corresponds to CoO and Co_3O_4 phases (both are paramagnetic at room temperature). In the thinnest sample (5 nm), *M* starts to increase immediately after voltage is applied. Because of this progressive increase in *M* with time, the ascending and descending branches of the loop cross each other. The increase of *M* is due to the formation of Co clusters resulting from the release of the O^{2-} ions from the magneto-ionic film into the electrolyte.[35,37] Remarkably, the signal reaches a steady-state value after the first *M*–*H* loop measurement (*i.e.*, during the first 35 min, red hysteresis loop). A similar result is obtained for the 36 nm thick sample. In contrast, the magnetization of the thicker Co_3O_4 films continues to increase after the first measurement is completed (*i.e.*, for times larger than 35 min). In the case of the thickest sample (230 nm), it takes up to 5 hours to reach a stable saturation magnetization (M_S). From these results it can be inferred that the magneto-ionic rates depend on film thickness (thinner cobalt oxide films result in faster rates), and the amount of generated magnetic signal (normalized per unit volume) is inversely proportional to the film thickness. Comparing the samples after M_S has stabilized, it is observed that the induced M_S increases with decreasing film thickness, while the coercivity (H_C) increases with increasing film thickness.

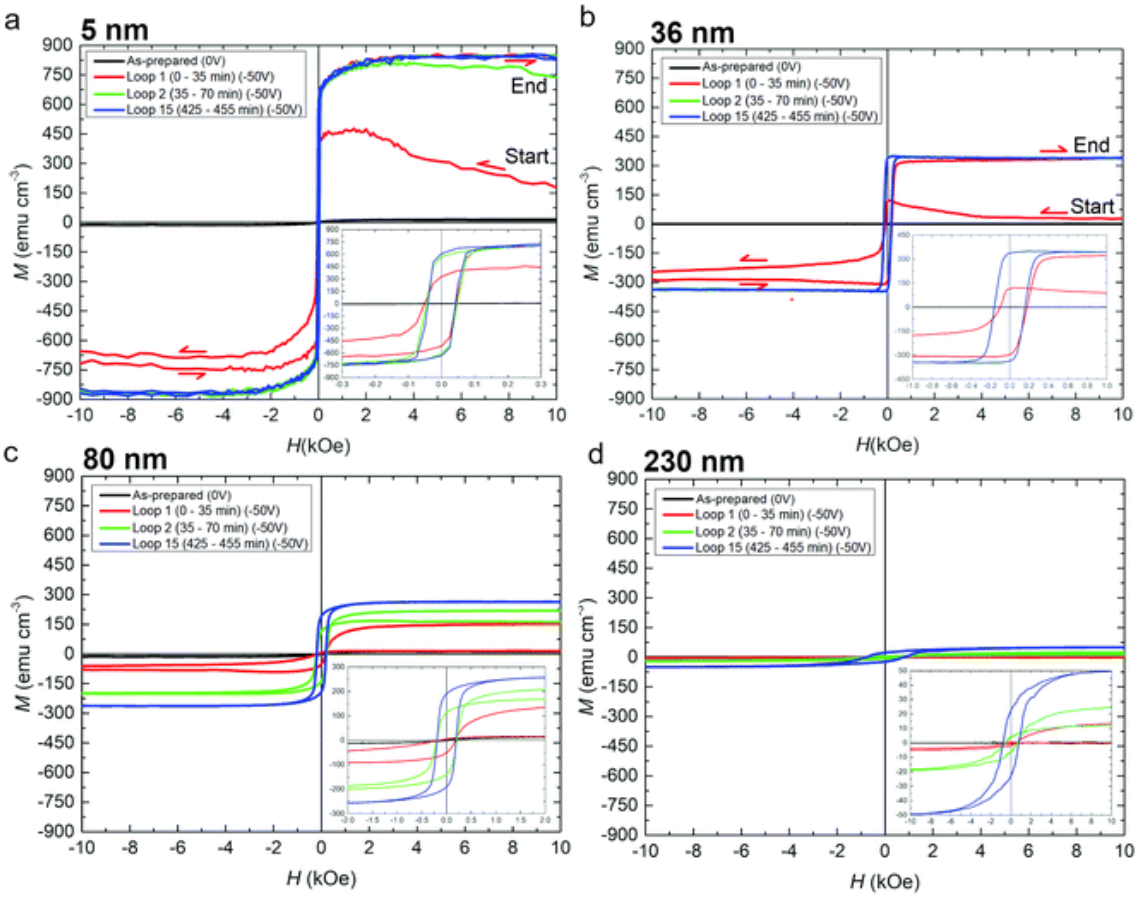

Fig. 2 Dependence of magneto-ionic effects on the cobalt oxide film thickness. Panels a–d show consecutive hysteresis loops corresponding to cobalt oxide films of 5, 36, 80 and 230 nm thickness, respectively, upon electrolyte gating (ΔV = −50 V) acquired using a vibrating sample magnetometer (magnetic field applied in-plane). Note that the hysteresis loops corresponding to the cobalt oxide film of 15 nm thickness are shown in Fig. S4.†

shows the dependence of the M_S and H_C as function of time, extracted from the ascending and descending branches of the measured hysteresis loops. The magnetization increases with time for all thicknesses, but it does so at a faster rate in thinner cobalt oxide films. In addition, the steady-state M_S value (once taking into account the normalization by the film thickness) of the 5 nm cobalt oxide film is about 18 times larger than the M_S of the 230 nm film (50 emu cm^{-3} *vs.* 900 emu cm^{-3}). This corroborates that magneto-ionic effects have a strong dependence on film thickness and are much more pronounced (and occur faster) in thinner transition-metal oxide films. The reason for this is two-fold: first, the generated electric field is larger for thinner cobalt oxide films (by a factor 230/5 = 46); second, in thinner films, O^{2-} ions have to travel shorter distances until they reach the propylene carbonate. Additionally, it must be noted that film composition can have some influence on the magneto-ionic performance, since thinner films (5 and 15 nm) are mainly CoO (as observed in Fig. 1b), whereas thicker films are a mixture of Co_3O_4 and CoO phases (36 nm) or predominantly Co_3O_4 (229 nm). While CoO can readily reduce to metallic Co by applying a negative voltage, the Co_3O_4 phase (which contains a mixture of Co^{2+} and Co^{3+} cations) can reduce either to metallic Co (Co^0) or undergo a partial reduction of the oxidation state (from Co^{3+} to Co^{2+}), resulting in a mixture of metallic Co + CoO, as was reported in previous works.[35] This also limits the amount of generated magnetic moment in the thicker films. The slightly weaker Co–O bond in CoO compared with Co_3O_4 also indicates that, under equivalent applied voltages, O magneto-ionics is faster in CoO than in Co_3O_4.[54–56]

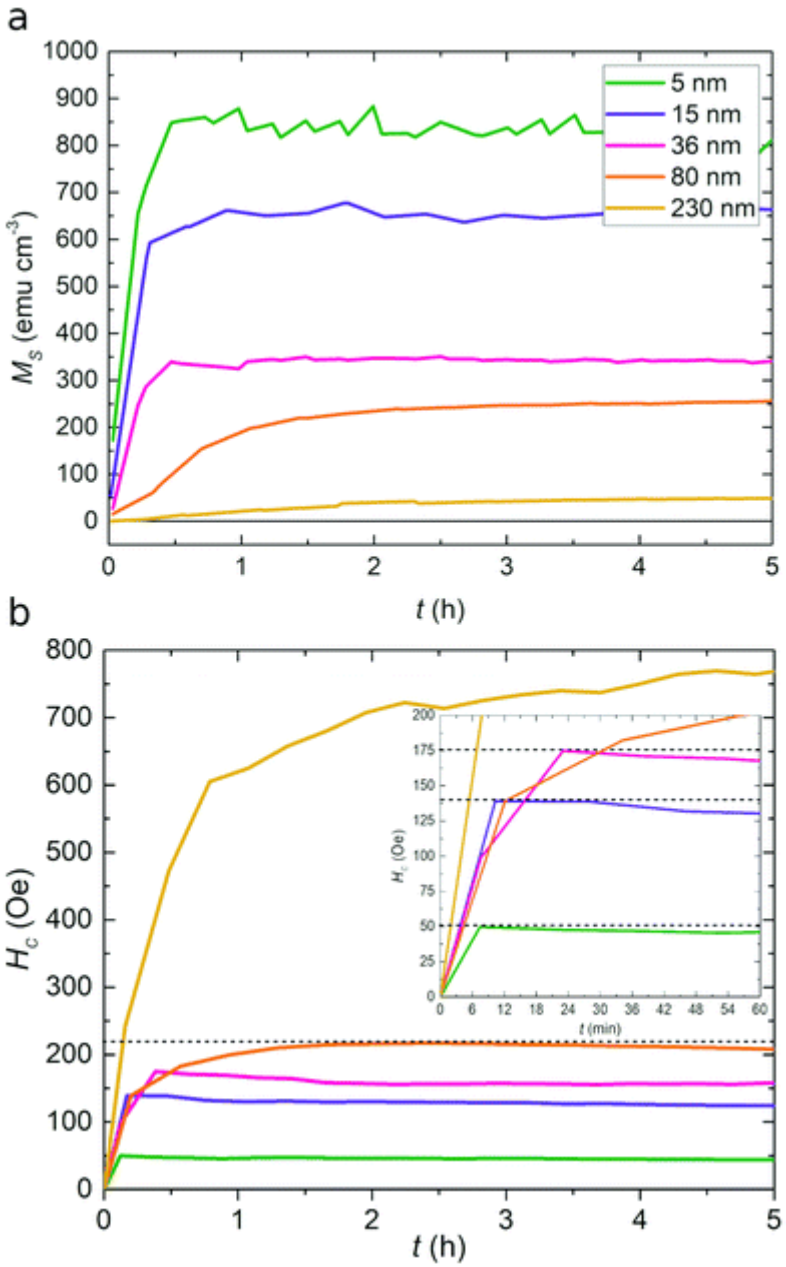

Fig. 3 Time evolution of (a) the saturation magnetization (M_S) and (b) the coercivity (H_C) for the various cobalt oxide film thicknesses with a zoom in corresponding to the first hour of time evolution of H_C.

The coercivity increases with actuation time for all films, reaching a maximum and then slightly decreasing as the actuation time is further increased (Fig. 3b) This is visible for all films except the 230 nm one, where the slight decrease of H_C would pressumably occur at higher actuation times. Interestingly, H_C and also the actuation time at which peak H_C is reached both increase for larger film thickness. This can be explained by the way Co clusters are generated during magneto-ionic actuation (Fig. 4a and b) and the well-known size dependence of coercivity in ferromagnetic particles (*i.e.*, H_C is known to exhibit a maximum as a function of particle size).[57] First, the system is paramagnetic ($t = t_0$). Short actuation times generate small Co clusters, sparsely embedded in the paramagnetic oxide matrix after some oxygen is removed. These clusters are likely to be

superparamagnetic due to their reduced size, with H_C nearly negligible. As the actuation time increases (*e.g.*, $t = t_1$), the Co clusters increase in size and eventually become single-domain ferromagnetic particles (with increasing H_C). For a fixed actuation time, the density of Co clusters is larger in thinner films, as evidenced by the larger M_S (Fig. 4a). For longer times ($t = t_2$), the size of the clusters increases, and they eventually become multi-domain (H_C decreases from the single-domain peak). This is likely to happen faster for thinner films, where the magneto-ionic effects are more pronounced. In thinner films, the inter-cluster distance also decreases (Fig. 4a), thus increasing the strength of dipolar interactions, which also tend to reduce H_C due to the collective switching of the magnetization in these interacting clusters. For Co, the single domain state is expected at 70 nm.[58] For a given ($t = t_2$) (where H_C already decreases in thinner films), Co clusters remain small and isolated (*i.e.*, with weaker dipolar interactions) in thicker films (Fig. 4b – t_2). This allows H_C to still further increase by subjecting the film to the action of voltage for longer times, thus explaining the shift in the maximum of H_C with actuation time shown in Fig. 3b. The analysis of HRTEM images of voltage-actuated thin Co oxide films (around 25 nm) reveals a higher density of Co clusters (Fig. S3†) than in thick (>100 nm) Co oxide films treated in a similar way.[35] The Co cluster size is in both cases in the range 3–6 nm. These observations are in qualitative agreement with the cartoon provided in Fig. 4 which explains the trends in coercivity as a function of film thickness and voltage application time.

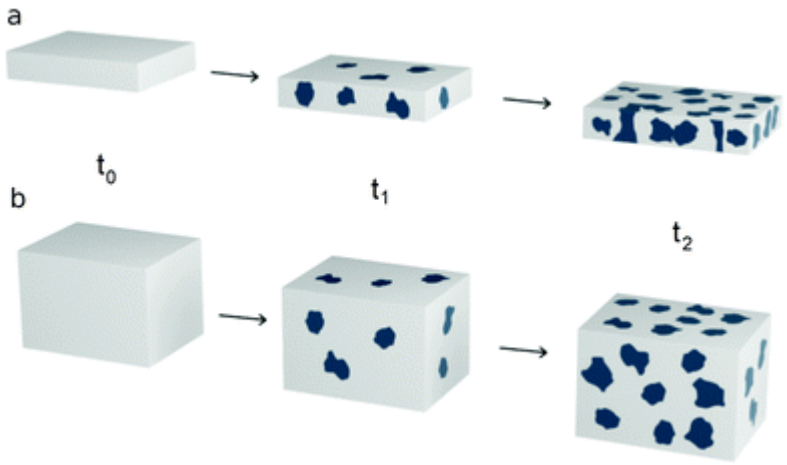

Fig. 4 Schematics of the evolution of the size and density of magneto-ionically generated Co clusters (dark regions) for a thin (a) and a thick (b) cobalt oxide film, respectively.

To better assess the magneto-ionic effects during the first stages of voltage application, *M vs.* time measurements under −50 V bias were performed while applying a constant magnetic field of 10 kOe (large enough to keep the generated ferromagnetic counterparts in a magnetically saturated state). This allows a more precise calculation of the activation time (*i.e.*, the time required to achieve a measurable generated magnetic moment, which in our setup is around 1 μemu), as well as the real magneto-ionic rate. As seen in Fig. 5a, the M_S reached after 33 minutes is, for all samples,

approximately the same as the one at the end of the first loop shown in Fig. 2. However, while M_S increases quickly in the thinner films (the activation time is lower than 1 second for the 5 nm cobalt oxide film), it takes between 10–100 s to reach a measurable M_S value in the thickest films.

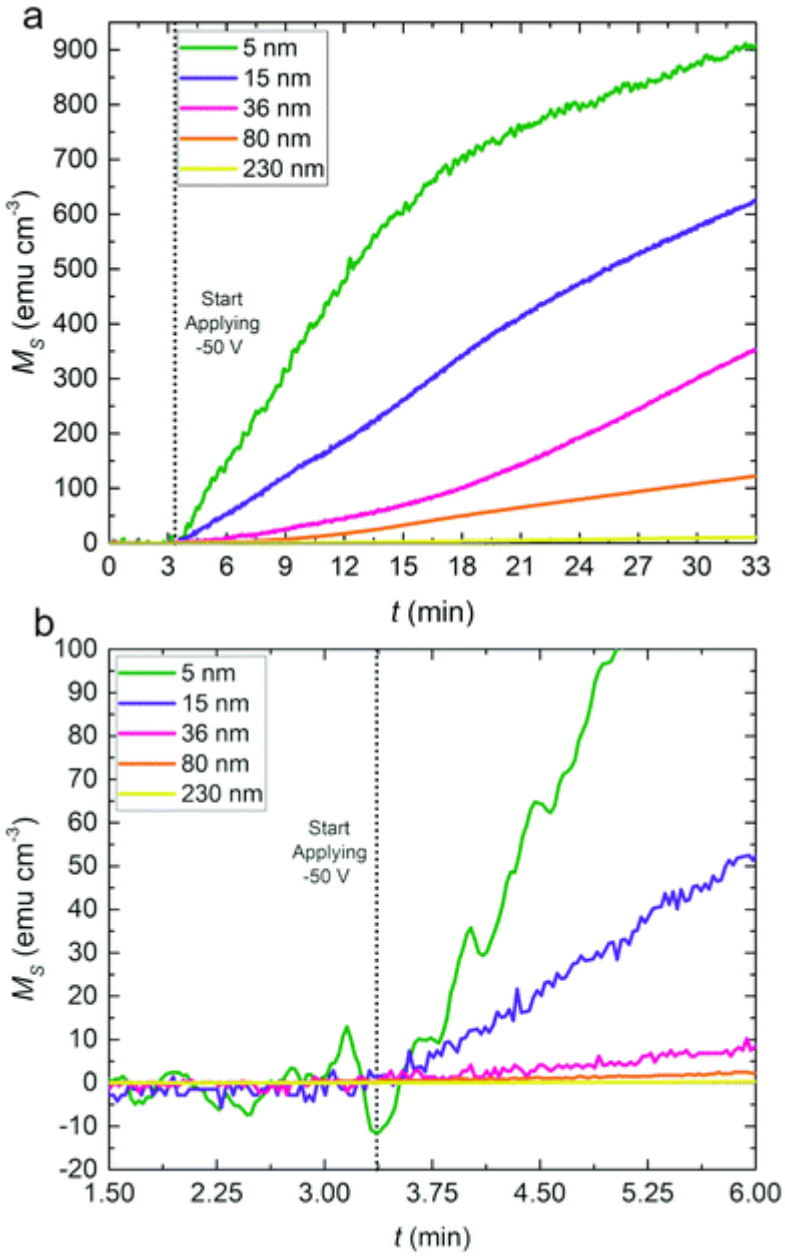

Fig. 5 (a) Time evolution of saturation magnetization (M_S) as a function of time for variable cobalt oxide film thickness, acquired while applying an in-plane magnetic field of 10 kOe. (b) Zoom in of the initial stages of magnetization generation to better illustrate the dissimilar activation times of the films.

Table 1 summarizes the steady-state magnetic properties (H_C, M_R, M_S and M_R/M_S, where M_R is the remanent magnetization and M_R/M_S the squareness ratio) of each film after long-term voltage actuation (as extracted from Fig. 2 and 5). The table also shows the maximum magneto-ionic motion rates obtained from the time derivative of the

saturation magnetization (*i.e.*, $(dM_S/dt)_{max}$ from Fig. S5†). The achieved magneto-ionic rates are drastically enhanced when the film thickness is reduced, from 0.5 emu cm^{-3} min^{-1} (for the 230 nm-thick film) to 67 emu cm^{-3} min^{-1} (for the 5 nm-thick film), approximately 3 times faster than that previously observed in 130 nm Co_3O_4 films.[37]

Table 1 Steady magnetic properties upon voltage actuation. H_C, M_S and M_R are extracted from Fig. 2, whereas the magneto-ionic rates and activation times are extracted from Fig. 5 and S5†

Thickness (nm)	H_C (Oe)	M_S (emu cm^{-3})	M_R (emu cm^{-3})	M_R/M_S (%)	Maximum magneto-ionic rate (emu cm^{-3} min^{-1})	Activation time (s)
5 ± 1	47 ± 1	852 ± 9	608 ± 6	71 ± 2	67 ± 2	<10 ± 4
15 ± 1	133 ± 3	660 ± 7	524 ± 5	79 ± 2	27.4 ± 0.8	22 ± 4
36 ± 1	178 ± 5	340 ± 3	337 ± 3	99 ± 2	19.5 ± 0.6	45 ± 4
80 ± 1	218 ± 5	264 ± 3	195 ± 2	74 ± 2	6.3 ± 0.2	52 ± 4
230 ± 1	782 ± 10	50.4 ± 0.5	23.2 ± 0.3	46 ± 1	0.52 ± 0.06	65 ± 4

Taking advantage of their fast magneto-ionic response, the thinnest cobalt oxide films (5 nm) were further investigated under pulsed voltage sequences, revealing remarkable neuromorphic functionalities. In particular, non-linear cumulative magneto-ionic effects (*i.e.*, learning neuromorphic capabilities) were induced in these films by subjecting them to −50 V/0 V pulse waves at frequencies ranging from 1 to 100 Hz. However, these results are not as one would anticipate *a priori*. For example, the M_S values obtained under 10 and 100 Hz pulsing are similar to those obtained using static voltage conditions (ΔV = −50 V). In contrast, the long-term M_S reached under 1 Hz pulsing is significantly lower (Fig. 6a). To understand this effect, the recovery curves (*i.e.*, M_S *vs.* time at ΔV = 0 V acquired after the measurements in Fig. 6a) were also recorded. A tendency for M_S to decrease with time is observed in all samples, akin to a forgetting neuromorphic function (Fig. 6b). However, while M_S steadily decreases with time after DC voltage actuation (suggesting a progressive re-oxidation of the magneto-ionically generated Co clusters), more complex dependencies are obtained after pulsed-voltage actuation. After DC voltage actuation, the re-oxidation process (partial recovery) is progressive and tends to stabilize after t = 1000 s; this is also the case when the pulsed voltage actuation is fast (*i.e.*, f = 100 Hz). However, when the actuation frequency is slower (*i.e.*, f = 1 Hz), the decrease of M_S with time is less obvious. This suggests that two-way O^{2-} ion migration effects (from the sample to the electrolyte and *vice versa*) may occur simultaneously once dynamic voltage actuation has stopped. In fact, at f = 1 Hz, partial recovery can also take place during the learning segment, during each of the pulse half-cycles when ΔV = 0. This explains why the increase of M_S under f = 1 Hz pulsing is less than samples treated under DC, 10 Hz pulsing, and 100 Hz pulsing (Fig. 6a), evidencing a trade-off between magnetization generation (ΔV = −50 V, voltage ON) and magnetization depletion due to partial recovery (ΔV = 0 V, voltage OFF) that scales with pulse duration.

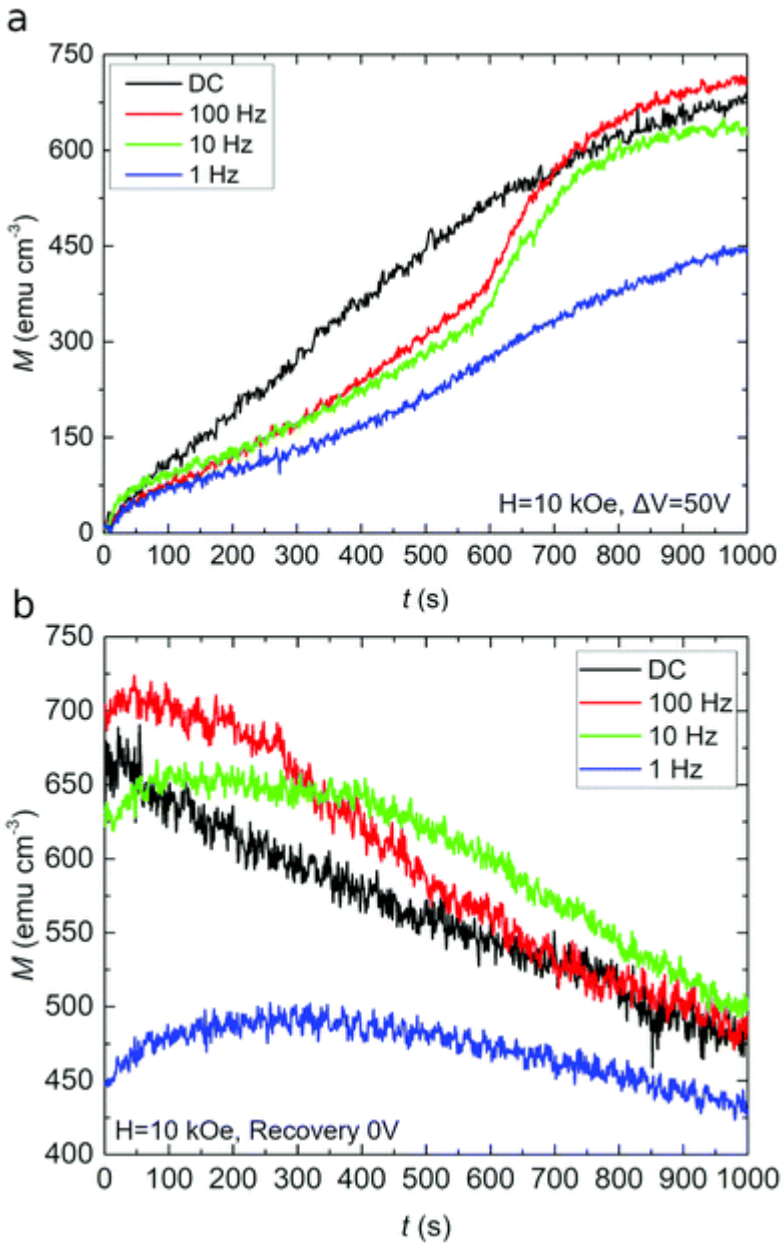

Fig. 6 Time evolution of M_S while applying an in-plane magnetic field of 10 kOe. (a) M_S *vs.* *t* during static (ΔV_{DC} = −50 V) and dynamic (pulsed) voltage actuation (applying −50 V/0 V at frequencies of 1 Hz, 10 Hz and 100 Hz). (b) shows the recovery experiments, while measuring M_S as a function of time with ΔV = 0 V.

Importantly, these experiments reveal that magneto-ionic motion can be induced in cobalt oxide films with pulses of 100 Hz, *i.e.*, with activation times of the order of 10^{-2} s. This is significantly faster than what is reported in most works on magneto-ionics relying on room-temperature O^{2-} ion migration,[20,21,24,35] and approaches the magneto-ionic rates reported in some H^+ magneto-ionic studies.[33,34]

The effects of recovery are also evident by measuring two consecutive hysteresis loops, under ΔV = 0 V, after actuating the cobalt oxide films for 1000 s under DC and pulsed conditions (Fig. 7). Large recovery effects are observed after DC actuation, where *M* progressively decreases with time during the first and second hysteresis loops.

The recovery decreases with decreasing pulse frequency. However, *M* reduces to a much lesser extent after actuation using voltage pulses of 1 Hz. This is in agreement with the results of Fig. 6b and can be understood as the result of partial recovery taking place during the OFF periods of magneto-ionic experiments at 1 Hz. For higher frequencies, the trade-off between magnetization generation (voltage ON) and magnetization depletion due to partial recovery (voltage OFF) is shifted towards the former, resulting in a larger 'learning' capacity and a reduced 'forgetting' process.

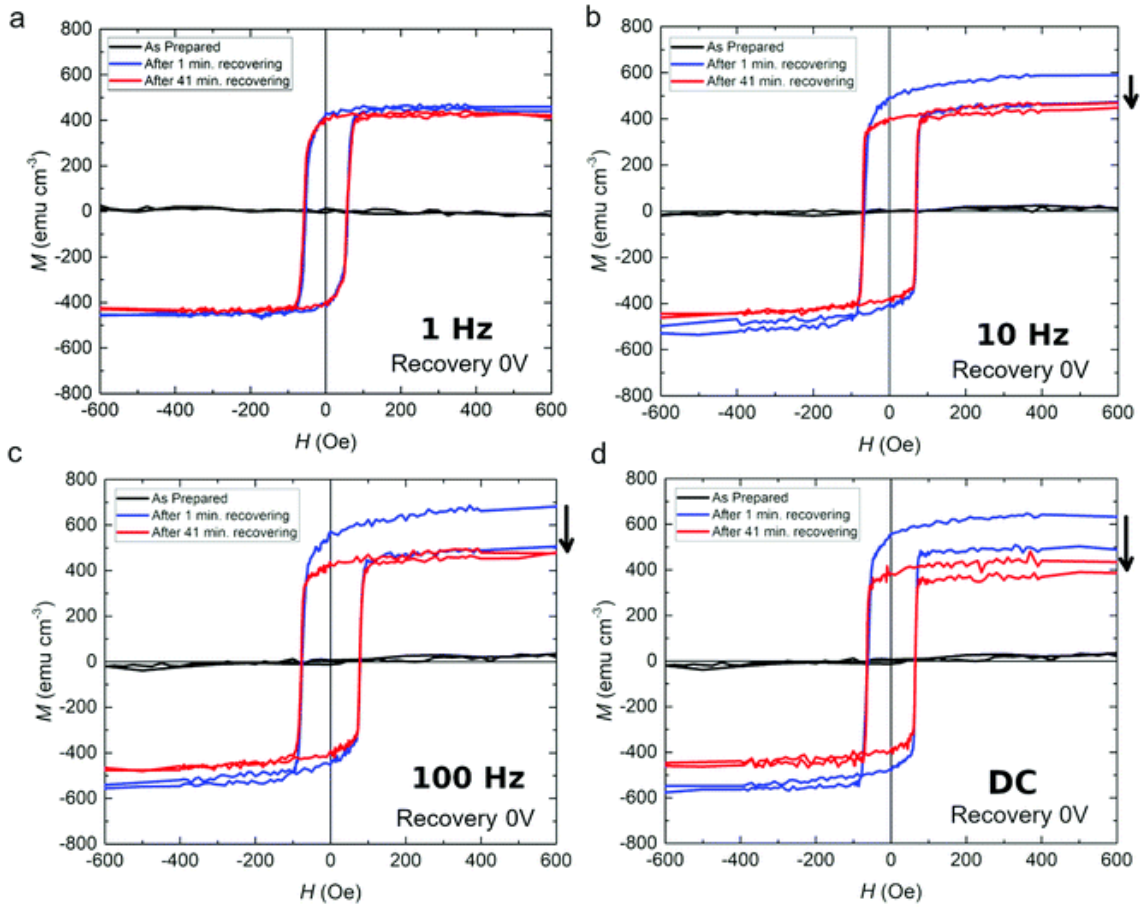

Fig. 7 Magnetic recovery effects evidenced by measuring two consecutive hysteresis loops after having actuated the cobalt oxide films for 1000 s using 50 V/0 V voltage pulses at frequencies of (a) 1 Hz, (b) 10 Hz and (c) 100 Hz. (d) the same recovery experiment after applying a DC voltage of −50 V for 1000 s.

These results provide evidence that magneto-ionic systems can emulate potentiation or 'learning' functionalities. Similar to the way the human brain works, repeated spiking (*i.e.*, high frequency voltage pulsing) allows for information retention, exhibiting spike-timing-dependent plasticity (*i.e.*, 'learning') analogous to the magneto-ionic generation of magnetization upon dynamic actuation.

To examine the reliability of the observed magneto-ionic effects in terms of endurance and cyclability, voltage pulses of −50 V and +50 V were repeatedly applied to the 5 nm-thick cobalt oxide film, 15 s in duration (sufficient to ensure measurable generation and suppression of the magnetization). The time dependence of the magnetic moment (*m*) is plotted in Fig. S6† together with the same kind of measurement

performed on a reference Si/Ti/Cu sample (without the cobalt oxide film). While clear changes are observed in the cobalt oxide film (blue curve), only non-periodic noise is observed in the reference substrate, thus confirming that the measured changes in *M* are not an artifact of the experimental setup, but a truly magneto-ionic effect. Remarkably, from the total *m* generated in the first cycle (4.42×10^{-6} emu), one can calculate the amount of Co generated. This magnetic moment corresponds to a total effective thickness of 0.89 nm of Co is created. In other words, about 18% of the pristine cobalt oxide is transformed to metallic Co during the first voltage pulse. This is much larger than the amount of Co generated in thicker films after long-term voltage application, which was calculated to be 6% in our previous works.[35] Fig. 8 shows the normalized magnetic moment (*i.e.*, *M*) together with the alternating voltage actuation as function of time. From Fig. 8 we can further resolve the activation time for magneto-ionic effect and it is down to <5 seconds (in agreed with Table 1).

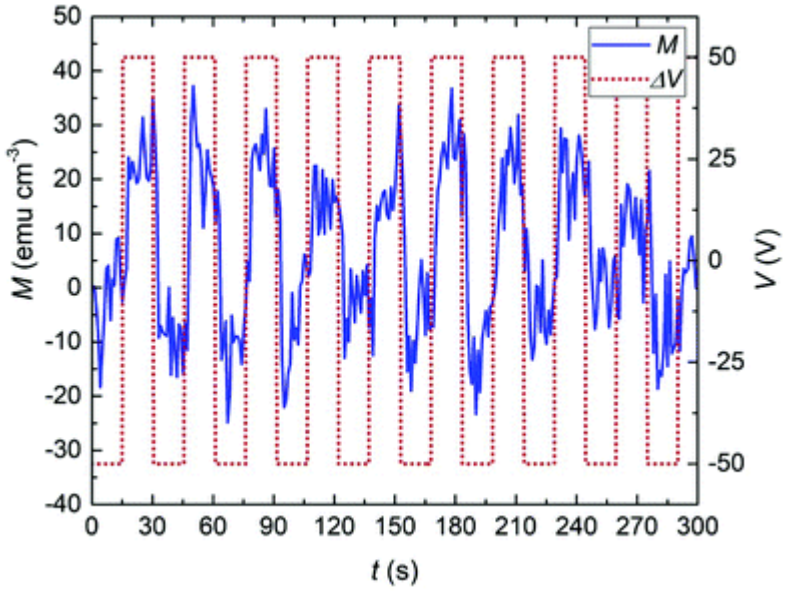

Fig. 8 Magneto-ionic cyclability of the cobalt oxide 5 nm-thick film under −50 V/+50 V voltage pulses of 15 s duration each, assessed from in-plane magnetic measurements while applying a magnetic field of 10 kOe. The superposition of the time evolution of the applied voltage (red discontinuous curve) and the magnetic moment (in blue) for the cobalt oxide film.

Conclusions

Our results reveal that the strength of magneto-ionic effects generated in electrolyte-gated paramagnetic cobalt oxide films exhibit a strong film-thickness dependence. After long-term application of a sufficiently strong DC voltage ($\Delta V = -50$ V), the generated magnetization in ultra-thin (5 nm) cobalt oxide films is almost 17 times larger than that of thick (230 nm) films. In turn, much faster magneto-ionic rates are obtained in the thinnest films, by a factor 134 times larger in the 5 nm films than for 230 nm films. Remarkably, prominent cumulative magneto-ionic effects (emulating potentiation and

plasticity effects of biological synapses) can be obtained by applying pulsed voltages. During dynamic experiments (*i.e.*, using −50 V/0 V square voltage pulses at frequencies in the range 1 Hz–100 Hz), the generated magnetization is smaller for lower frequencies. This can be understood by considering the interplay between potentiation and *M* depletion effects that occurs during the ON and OFF time periods at sufficiently slow frequencies. Interestingly, for the thin 5 nm cobalt oxide films, transitions from paramagnetic to ferromagnetic states are generated in sub-second time intervals. Cumulative magneto-ionic effects at 100 Hz indicate that activation times are on the order of 10^{-2} s in the thinner films, among the fastest reported so far in magneto-ionic systems relying on O^{2-} ion migration. Our results represent an important contribution towards the applicability of magneto-ionics in practical applications such as neuromorphic computing, which operate at speeds similar to the ones achieved in this work.[59]

Conflicts of interest

There are no conflicts to declare.

Acknowledgements

This work has received funding from the European Unions Horizon 2020 Research and Innovation Programme BeMAGIC under the Marie Sklodowska-Curie grant agreement No 861145. Financial support by the European Research Council (SPIN-PORICS 2014-Consolidator Grant, Agreement No. 648454, and MAGIC-SWITCH 2019-Proof of Concept Grant, Agreement No. 875018), the Spanish Government (MAT2017-86357-C3-1-R, PID2020-116844RB-C21), the Generalitat de Catalunya (2017-SGR-292 and 2018-LLAV-00032) and the European Regional Development Fund (MAT2017-86357-C3-1-R and 2018-LLAV-00032) is acknowledged. The authors would like to thank João Lucas (jgbl89@gmail.com) for the illustrations. XAS experiments were performed at BL29-BOREAS beamline at ALBA Synchrotron with the collaboration of ALBA staff. E. M. is a Serra Húnter Fellow.

References

1. M. Skipper, *Nature*, 2018, **554**, 145–146.
2. X. Xu, Y. Ding, S. X. Hu, M. Niemier, J. Cong, Y. Hu and Y. Shi, *Nat. Electron.*, 2018, **1**, 216–222.
3. S. Kasap and P. Capper, *Springer Handbook of Electronic and Photonic Materials*, Springer Handbooks, 2nd edn, 2017, pp. 1–21536.
4. O. Vaughan, *Nat. Electron.*, 2018, **1**, 205.
5. W. A. Wulf and S. A. McKee, *ACM SIGARCH Comput. Archit. News*, 1995, vol. 23, pp. 20–24.
6. D. Ielmini and S. Ambrogio, *Nanotechnology*, 2020, **31**, 092001.
7. R. Islam, H. Li, P.-Y. Chen, W. Wan, H.-Y. Chen, B. Gao, H. Wu, S. Yu, K. Saraswat and H.-S. P. Wong, *J. Phys. D: Appl. Phys.*, 2019, **52**, 113001.
8. J. Park, *Electronics*, 2020, **9**, 1–16.

9. C. D. James, J. B. Aimone, N. E. Miner, C. M. Vineyard, F. H. Rothganger, K. D. Carlson, S. A. Mulder, T. J. Draelos, A. Faust, M. J. Marinella, J. H. Naegle and S. J. Plimpton, *Biol. Inspired Cogn. Archit.*, 2017, **19**, 49–64.
10. R. Douglas, M. Mahowald and C. Mead, *Annu. Rev. Neurosci.*, 1995, **18**, 255–281.
11. W. Zhang, R. Mazzarello, M. Wuttig and E. Ma, *Nat. Rev. Mater.*, 2019, **4**, 150–168.
12. M. A. Galin, E. A. Borodianskyi, V. V. Kurin, I. A. Shereshevskiy, N. K. Vdovicheva, V. M. Krasnov and A. M. Klushin, *Phys. Rev. Appl.*, 2018, **9**, 54032.
13. P. Gkoupidenis, N. Schaefer, B. Garlan and G. G. Malliaras, *Adv. Mater.*, 2015, **27**, 7176–7180.
14. M. Zahedinejad, A. A. Awad, S. Muralidhar, R. Khymyn, H. Fulara, H. Mazraati, M. Dvornik and J. Åkerman, *Nat. Nanotechnol.*, 2020, **15**, 47–52.
15. J. Torrejon, M. Riou, F. A. Araujo, S. Tsunegi, G. Khalsa, D. Querlioz, P. Bortolotti, V. Cros, K. Yakushiji, A. Fukushima, H. Kubota, S. Yuasa, M. D. Stiles and J. Grollier, *Nature*, 2017, **547**, 428–431.
16. V. Milo, C. Zambelli, P. Olivo, E. Pérez, M. K. Mahadevaiah, O. G. Ossorio, C. Wenger and D. Ielmini, *APL Mater.*, 2019, **7**, 081120.
17. D. Ielmini, Z. Wang and Y. Liu, *APL Mater.*, 2021, **9**, 050702.
18. J. Del Valle, J. G. Ramírez, M. J. Rozenberg and I. K. Schuller, *J. Appl. Phys.*, 2018, **124**, 211101.
19. C. Song, B. Cui, F. Li, X. Zhou and F. Pan, *Prog. Mater. Sci.*, 2017, **87**, 33–82.
20. A. Molinari, H. Hahn and R. Kruk, *Adv. Mater.*, 2019, **31**, 1806662.
21. C. Navarro-Senent, A. Quintana, E. Menéndez, E. Pellicer and J. Sort, *APL Mater.*, 2019, **7**, 030701.
22. Y. Cheng, B. Peng, Z. Hu, Z. Zhou and M. Liu, *Phys. Lett. A*, 2018, **382**, 3018–3025.
23. R. Mishra, D. Kumar and H. Yang, *Phys. Rev. Appl.*, 2019, **11**, 054065.
24. M. Nichterwitz, S. Honnali, M. Kutuzau, S. Guo, J. Zehner, K. Nielsch and K. Leistner, *APL Mater.*, 2021, **9**, 030903.
25. W. Kleemann and C. Binek, *Springer Tracts Mod. Phys.*, 2013, **246**, 163–187.
26. J. M. Hu, C. W. Nan and L. Q. Chen, *Natl. Sci. Rev.*, 2019, **6**, 621–624.
27. D. Hayakawa, A. Obinata, K. Miwa, S. Ono, T. Hirai, T. Koyama and D. Chiba, *AIP Adv.*, 2016, **6**, 115305.
28. W. Lin, N. Lei, N. Vernier, G. Agnus, J. P. Adam, S. Eimer, T. Devolder, P. Lecoeur and D. Ravelosona, *Thin Solid Films*, 2013, **533**, 70–74.
29. Z. Hu, X. Wang, T. Nan, Z. Zhou, B. Ma, X. Chen, J. G. Jones, B. M. Howe, G. J. Brown, Y. Gao, H. Lin, Z. Wang, R. Guo, S. Chen, X. Shi, W. Shi, H. Sun, D. Budil, M. Liu and N. X. Sun, *Sci. Rep.*, 2016, **6**, 32408.
30. W. Du, M. Liu, H. Su, H. Zhang, B. Liu, H. Meng, G. Xu, R. Peng and X. Tang, *Appl. Phys. Lett.*, 2020, **117**, 222401.
31. D. A. Links, *Nanoscale*, 2012, **4**, 3218–3227.
32. U. Bauer, L. Yao, A. J. Tan, P. Agrawal, S. Emori, H. L. Tuller, S. Van Dijken and G. S. Beach, *Nat. Mater.*, 2015, **14**, 174–181.
33. A. J. Tan, M. Huang, C. O. Avci, F. Büttner, M. Mann, W. Hu, C. Mazzoli, S. Wilkins, H. L. Tuller and G. S. Beach, *Nat. Mater.*, 2019, **18**, 35–41.

34. K. Y. Lee, S. Jo, A. J. Tan, M. Huang, D. Choi, J. H. Park, H. I. Ji, J. W. Son, J. Chang, G. S. Beach and S. Woo, *Nano Lett.*, 2020, **20**, 3435–3441.
35. A. Quintana, E. Menéndez, M. O. Liedke, M. Butterling, A. Wagner, V. Sireus, P. Torruella, S. Estradé, F. Peiró, J. Dendooven, C. Detavernier, P. D. Murray, D. A. Gilbert, K. Liu, E. Pellicer, J. Nogues and J. Sort, *ACS Nano*, 2018, **12**, 10291–10300.
36. J. de Rojas, A. Quintana, A. Lopeandía, J. Salguero, B. Muñiz, F. Ibrahim, M. Chshiev, A. Nicolenco, M. O. Liedke, M. Butterling, A. Wagner, V. Sireus, L. Abad, C. J. Jensen, K. Liu, J. Nogués, J. L. Costa-Krämer, E. Menéndez and J. Sort, *Nat. Commun.*, 2020, **11**, 5871.
37. J. de Rojas, A. Quintana, A. Lopeandía, J. Salguero, J. L. Costa-Krämer, L. Abad, M. O. Liedke, M. Butterling, A. Wagner, L. Henderick, J. Dendooven, C. Detavernier, J. Sort and E. Menéndez, *Adv. Funct. Mater.*, 2020, **30**, 2003704.
38. L. Herrera Diez, R. Kruk, K. Leistner and J. Sort, *APL Mater.*, 2021, **9**, 050401.
39. K. Zheng, F. Sun, J. Zhu, Y. Ma, X. Li, D. Tang, F. Wang and X. Wang, *ACS Nano*, 2016, **10**, 7792–7798.
40. D. A. Gilbert, A. J. Grutter, E. Arenholz, K. Liu, B. J. Kirby, J. A. Borchers and B. B. Maranville, *Nat. Commun.*, 2016, **7**, 12264.
41. D. A. Gilbert, J. Olamit, R. K. Dumas, B. J. Kirby, A. J. Grutter, B. B. Maranville, E. Arenholz, J. A. Borchers and K. Liu, *Nat. Commun.*, 2016, **7**, 11050.
42. M. Cialone, A. Nicolenco, S. Robbennolt, E. Menéndez, G. Rius and J. Sort, *Adv. Mater. Interfaces*, 2021, **8**, 2001143.
43. J. M. Hu and C. W. Nan, *APL Mater.*, 2019, **7**, 080905.
44. K. L. Wang, H. Lee and P. K. Amiri, *IEEE Trans. Nanotechnol.*, 2015, **14**, 992–997.
45. H. Cai, W. Kang, Y. Wang, L. A. De Barros Naviner, J. Yang and W. Zhao, *Appl. Sci.*, 2017, **7**, 929.
46. K. Jabeur, G. Pendina and G. Prenat, *Electr. Electron. Eng. An Int. J.*, 2017, **6**, 1–9.
47. S. Manipatruni, D. E. Nikonov, C. C. Lin, T. A. Gosavi, H. Liu, B. Prasad, Y. L. Huang, E. Bonturim, R. Ramesh and I. A. Young, *Nature*, 2019, **565**, 35–42.
48. J. de Rojas, J. Salguero, F. Ibrahim, M. Chshiev, A. Quintana, A. Lopeandia, M. O. Liedke, M. Butterling, E. Hirschmann, A. Wagner, L. Abad, J. L. Costa-Krämer, E. Menéndez and J. Sort, *ACS Appl. Mater. Interfaces*, 2021, **13**, 30826–30834.
49. A. Barla, J. Nicolás, D. Cocco, S. M. Valvidares, J. Herrero-Martín, P. Gargiani, J. Moldes, C. Ruget, E. Pellegrin and S. Ferrer, *J. Synchrotron Radiat.*, 2016, **23**, 1507–1517.
50. F. C. Wu, S. W. Hsu, H. L. Cheng, W. Y. Chou and F. C. Tang, *J. Phys. Chem. C*, 2013, **117**, 8691–8696.
51. Q. He, Q. Li, S. Khene, X. Ren, F. E. López-Suárez, D. Lozano-Castelló, A. Bueno-López and G. Wu, *J. Phys. Chem. C*, 2013, **117**, 8697–8707.
52. T. Takada, Y. Bando, N. Yamamoto and K. Nagasawa, *Jpn. J. Appl. Phys.*, 1969, **8**, 619–619.
53. K. M. Nam, J. H. Shim, D. W. Han, H. S. Kwon, Y. M. Kang, Y. Li, H. Song, W. S. Seo and J. T. Park, *Chem. Mater.*, 2010, **22**, 4446–4454.

54. R. Robie and B. S. Hemingway, *Thermodynamic Properties of Minerals and Related Substances at 298.15K and 1 Bar*, 1995, pp. 1–461.
55. L. Glasser and D. A. Sheppard, *Inorg. Chem.*, 2016, **55**, 7103–7110.
56. M. W. Chase, *J. Phys. Chem. Ref. Data, Monogr.*, 1998, **4**, 1–1951.
57. E. F. Kneller and F. E. Luborsky, *J. Appl. Phys.*, 1963, **34**, 656–658.
58. D. L. Leslie-Pelecky and R. D. Rieke, *Chem. Mater.*, 1996, **8**, 1770–1783.
59. J. J. Harris, R. Jolivet and D. Attwell, *Neuron*, 2012, **75**, 762–777.